

New Experimental Limits on Macroscopic Forces Below 100 Microns

Joshua C. Long*, Hilton W. Chan**, Allison B. Churnside,
Eric A. Gulbis, Michael C. M. Varney, and John C. Price
Department of Physics, University of Colorado, Boulder CO

(Dated: September 30, 2002)

Abstract

Results of an experimental search for new macroscopic forces with Yukawa range between 5 and 500 microns are presented. The experiment uses 1 kHz mechanical oscillators as test masses with a stiff conducting shield between them to suppress backgrounds. No signal is observed above the instrumental thermal noise after 22 hours of integration time. These results provide the strongest limits to date between 10 and 100 microns, improve on previous limits by as much as three orders of magnitude, and rule out half of the remaining parameter space for predictions of string-inspired models with low-energy supersymmetry breaking. New forces of four times gravitational strength or greater are excluded at the 95% confidence level for interaction ranges between 200 and 500 microns.

* Present address: Los Alamos Neutron Science Center, LANSCE-3, MS-H855, Los Alamos, NM 87545, USA

** Present address: Physics Department, Stanford University, Stanford, CA 94305, USA

I. INTRODUCTION

Experimental tests of Newtonian gravity and searches for new weak forces in addition to gravity have been conducted over length scales ranging from light-years down to laboratory distances. Based on recent results [1] and reviews [2], new forces with strength weaker than or comparable to gravity have been excluded over distances ranging between 200 μm and a light-year. To date, only the single experiment in Ref. [1] has attained gravitational sensitivity below 1 mm, and limits on the strength of new interactions increase very rapidly below 100 μm [3]. The sub-millimeter range attracts continuing experimental interest because many recent theoretical attempts at the unification of fundamental forces predict specific new phenomena in this regime. We present the results of an experiment which has attained a maximum sensitivity of about four times gravitational strength above 200 μm , and which provides the most sensitive limits on new forces between 10 and 100 microns.

Results from experimental searches for new macroscopic forces are most commonly parameterized by a Yukawa interaction. The potential due to gravity and an additional Yukawa-type force between two mass densities $\rho_1(\vec{r}_1)$ and $\rho_2(\vec{r}_2)$ can be written

$$V = - \int d\vec{r}_1 \int d\vec{r}_2 \frac{G\rho_1(\vec{r}_1)\rho_2(\vec{r}_2)}{r_{12}} [1 + \alpha \exp(-r_{12}/\lambda)], \quad (1)$$

where G is the Gravitational constant, r_{12} is the distance between \vec{r}_1 and \vec{r}_2 , α is the strength of the Yukawa interaction relative to gravity, and λ is the range. Current experimental limits on α between 1 μm and 1 cm are shown in Fig. 7, together with several recent theoretical predictions of new phenomena.

All previously published limits in Fig. 7 (bold, dashed curves) are obtained from torsion balance experiments. These curves represent 95% confidence level limits with the exception of the result from the Irvine 2–5 cm null experiment [4], which is a 1 σ limit. The torsion balance experiment at the University of Washington has attained gravitational sensitivity or better for ranges above 200 μm [1]. Below 20 μm the best previous limit is derived from the Casimir force measurement by Lamoreaux [5]; the curve shown in Fig. 7 is based on the analysis by the authors [6, 7]. From the figure, the previous experimental limits allow for forces in nature several million times stronger than gravity at ranges as large as 20 μm .

A. Motivation

In addition to the unexplored parameter space, there are many specific motivations to search for new effects below $100 \mu\text{m}$ [8]. Several arise from the decades-long effort to describe gravity and the other fundamental interactions in a unified theoretical framework. The leading candidates for such a theory are string or M theories, which must be formulated in more than three spatial dimensions. In the traditional view, the extra dimensions are taken to be compactified on a scale on the order of the Planck length ($L_P \approx 10^{-35}$ m or $L_P^{-1} \approx 10^{19}$ GeV), a fundamental scale at which the unification is expected to occur. Recently, a class of models has been discovered in which the unification can occur at much lower energies, near the weak scale ($L_W^{-1} \approx 1$ TeV) [9]. In this picture, perhaps the most frequently cited development in particle physics in recent years, the discrepancy between the Planck scale and the weak scale (the so-called hierarchy problem) is removed as a consequence of some of the extra dimensions remaining large and accessible only to gravity, with the Standard Model fields confined to the usual three dimensions [10]. The size R of the extra dimensions is given by $R^n = L_W^{2+n}/L_P^2$, where n is the number of compact dimensions. For $n = 1$, $R \approx 10^{13}$ m, clearly ruled out by astrophysics. However, the choice of $n = 2$ implies $R \approx 1$ mm, with the consequence that the gravitational potential will behave according to a $1/r^3$ law below this scale. As the scale R is approached from above, Yukawa corrections are predicted; the model illustrated in Fig. 7 predicts $\alpha = 4$ [11].

Another class of predictions arises in superstring theories in which supersymmetry (SUSY) is broken at low energies. These models are of interest as unification scenarios that account for the absence of flavor-changing neutral currents. Superstring theories generally contain gravitationally-coupled scalar fields called moduli, which are massless at the string scale but which can acquire mass from the same process which breaks SUSY. For models in which SUSY is broken by a gauge-mediated process between 10 and 100 TeV, the moduli acquire masses at the sub-eV level corresponding to interaction ranges between $100 \mu\text{m}$ and 10 cm, with values of α as high as 10^6 [12]. Predictions for the largest such effects (for the moduli which couple to the strange quark and gluon) with the uncertainties are shown in Fig. 7. In a related model (radius modulus) in which SUSY is broken near 1 TeV via weak-scale compactification [13], the moduli can acquire Compton wavelengths in the range from $10 \mu\text{m}$ to 1 mm. The associated strength is predicted to be $\alpha = 1/3$, as

shown in Fig. 7.

The dilaton is another scalar field predicted by string theories, which can also acquire mass from SUSY breaking. Due to its more universal couplings, it is expected to acquire a mass too large to be observable in the scenario in Ref. [12], but other authors take the dilaton mass to be an unknown parameter. The estimated coupling for the dilaton from Ref. [14] is shown in Fig. 7, where previous experimental limits exclude a mass less than about 8×10^{-3} eV; more recent calculations can be found in Ref. [15].

The axion, a light pseudoscalar boson motivated by the strong CP problem of the Standard Model, is also predicted to mediate macroscopic forces. Astrophysical and laboratory bounds have left an allowed window for the axion mass corresponding to $200 \mu\text{m} < \lambda < 20 \text{ cm}$ [16]. The coupling of the associated long-range force between unpolarized test masses is constrained by measurements of the neutron electric dipole moment to the region indicated in Fig. 7. For pseudoscalars which are not derivative coupled (unlike the axion), double exchange leads to a $1/r^3$ potential between unpolarized test masses; short range experiments may set better limits on pseudoscalars via this effect [17].

Additional predictions are motivated by the cosmological constant (Λ) problem, the discrepancy between the observed flatness of the universe versus the extreme curvature expected from the vacuum energy contributions of the Standard Model fields. Recent models [18, 19] assert that if a sufficient fraction of the energy density in the universe is in the form of vacuum energy, consistency with local field theory implies the existence of new interacting quanta with mass on the order of $\Lambda^{1/4}$. The predictions in Fig. 7 are derived from the conservative assumption of cosmological vacuum energy density ρ_Λ in the range $0.1\rho_c < \rho_\Lambda < \rho_c$, where ρ_c is the critical density of the universe.

II. EXPERIMENT

The present experiment is illustrated in Fig. 1. The test masses consist of a planar resonant detector mass and a planar source mass driven at the detector resonant frequency. This geometry is chosen to concentrate as much test mass density as possible at the length scale of interest. It is also largely null with respect to $1/r^2$ forces and so is effective in suppressing the Newtonian background in the context of a new force search. The source mass consists of a $35 \text{ mm} \times 7 \text{ mm} \times 0.305 \text{ mm}$ node-mounted tungsten reed. It is driven

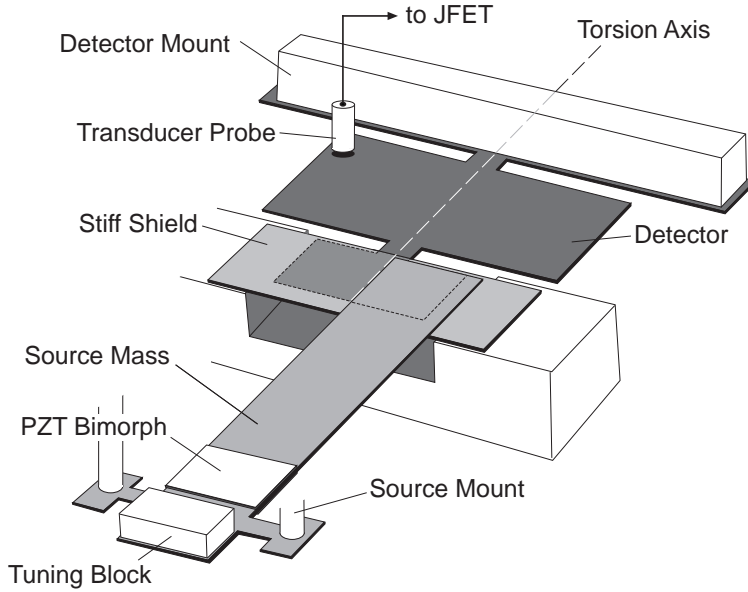


FIG. 1: Central components of the apparatus

at its second cantilever mode by a PZT bimorph at a frequency carefully matched to the 1 kHz resonant frequency of a normal mode of the detector mass. The detector mass consists of a 0.195 mm thick tungsten torsional oscillator of a double-rectangle design. The small rectangle measures 11.455 mm \times 5.080 mm. For the resonant mode of interest (the 5th normal mode) the two rectangular sections counter-rotate about the torsional axis, with most of the amplitude confined to the motion of the small rectangle. This double-torsional arrangement provides significant isolation of the small rectangle from the detector mount, reducing mode damping [20]. When data are collected, the front edge of the source mass is aligned with the back edge of the small detector rectangle, and a long edge of the source is aligned above the detector torsion axis. This geometry (called “fiducial” below) maximizes the on-resonance torque on the detector if a mass-coupled force is present between the source and detector.

A stiff conducting shield suspended between the test masses suppresses electrostatic and acoustic backgrounds. The shield consists of a 0.060 mm thick sapphire plate with a 100 nm gold plating. The shield is mounted on a brass support and secured on opposite ends with epoxy.

The test masses and shield support are each suspended from modified optical mirror mounts, which are used as a tilt stages to level each element in the horizontal plane. Each

tilt stage is in turn mounted to the bottom segment of a vibration isolation stack. Each stack consists of five solid brass disks connected by fine steel wires, as described in detail elsewhere [21]. At the 1 kHz operational frequency of the experiment, each stack provides an attenuation of approximately 200 dB. The vibration isolation stacks of the source and detector masses are suspended from inverted 3-axis micrometer stages, which provide full translation control. The relative positions and coplanarity of the test masses and shield are ascertained by touching the elements against each other, or against a series of 0.5 mm diameter sapphire hemispheres attached to small rods at the end of the shield support.

To further reduce acoustic backgrounds, the apparatus is placed in a 75 liter vacuum bell jar, which is pumped to a pressure of approximately 2×10^{-7} torr with a liquid nitrogen-trapped diffusion pump. In order to isolate the (non-magnetic) central apparatus from stray fields generated in the steel pump components, the bell jar is connected to the diffusion pump via a 1 m long, 10 cm diameter aluminum riser. The position-control micrometer stages are manually operated with torque rods which exit the bell jar via rotary feedthroughs.

In the absence of electromagnetic, acoustic, and vibrational backgrounds, the experiment is limited by thermal noise due to dissipation in the detector mass. To reduce this dissipation, the detector mass is annealed at 1300 °C for several hours in an induction furnace under a helium atmosphere before installation in the bell jar. This is observed to increase the detector mechanical quality factor (Q) typically by factors of 5 or more.

The detector temperature is stabilized with an electronic temperature controller using a silicon diode sensor and resistive heating element mounted to the bottom stage of the detector vibration isolation stack. The temperature is maintained at 305 K with fluctuations of about 0.1 K.

A. Readout

The detector readout electronics and source mass PZT drive are illustrated in Fig. 2. Oscillations of the detector mass are read out with a capacitive transducer. The capacitive transducer probe consists of a 2.5 mm diameter brass cylinder supported with its flat end approximately 0.1 mm above a rear corner of the large rectangle of the detector mass. The probe is biased at 200 V through a 100 G Ω resistor, whose value must be large to reduce current noise. The front end of the preamplifier consists of an SK152 JFET located in a small

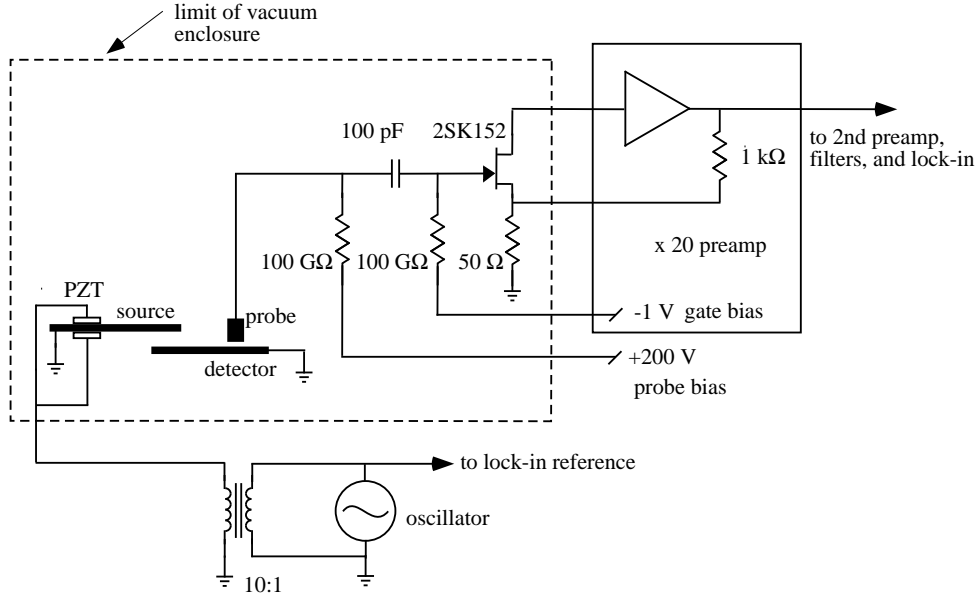


FIG. 2: Major components of the detector readout and PZT drive

box immediately above the detector oscillator. The 100 mK noise temperature of the SK152 preamplifier ensures that this circuit is more than sufficient for detecting the 300 K thermal oscillations (amplitude ≈ 100 fm) of the detector mass. The JFET preamplifier is followed by a second preamplifier (Stanford Research SR560), filters, and finally a two phase lock-in amplifier. The total voltage gain from the capacitive probe to the lock-in input is about 1600. A crystal-controlled oscillator provides a reference signal for the lock-in amplifier and drives the source mass PZT through a 1:10 step-up transformer.

III. DATA SAMPLE

A. Force Measurement Data

The data were recorded in 108 “cycles” over five days. Each cycle consists of 7 runs containing both force measurement data and diagnostic data. The diagnostic data are used to continually monitor the performance of the instrument. For all runs the bandwidth of the lock-in amplifier was set to 250 mHz (roughly 5 times the width of the detector resonance) to include the noise power of the detector thermal oscillations, which is used for calibration. A data sampling rate of 1 Hz was used, corresponding to an over-sampling of about a factor of 10.

Within each cycle, the runs were taken in the following order: First, a stable dc bias (usually 5–10 V) was applied to the shield to induce a large resonant electrostatic signal. A run of 120 samples was taken with the PZT drive frequency set 30 mHz below the approximate value of the detector resonant frequency. Four subsequent runs were taken, each with the PZT drive frequency incremented by 15 mHz relative to the previous run in order to display the detector resonance. The precise value of the detector resonant frequency was determined from the five biased runs, and was then used as the drive frequency for the next run of the cycle. The shield was then grounded and a run of 720 samples (12 minutes) was recorded. This was followed by a shorter run of 288 samples (4.8 minutes) taken with the PZT drive set to 1171.000 Hz (at least 2 Hz below the detector resonance), in order to monitor the system for non-resonant systematic offsets. The entire cycle was repeated indefinitely until an intervention to service the experiment was necessary. A total of 108 such cycles were acquired yielding a total of 77760 on-resonance samples.

A plot of the data from the biased diagnostic runs is shown in Fig. 3 (only data from 10 consecutive cycles are shown for clarity). The signals from the two phase-quadrature channels of the lock-in amplifier are plotted against each other to show the phase behavior of the signal with drive frequency. In all cycles, the signal maximizes at very nearly the same phase and magnitude, indicating good stability of the detector resonant frequency, source mass amplitude, and system gain.

Fig. 4 shows histograms of the on- and off-resonance unbiased data. The plots combine data from all 108 on-resonance and off-resonance runs, each plot displaying data from a single channel of the lock-in amplifier. The data exhibit smooth gaussian behavior centered about common means, as expected in the exclusive presence of detector thermal noise and amplifier noise. The widths of the distributions of the on-resonance data (left-hand plots in Fig. 4) are roughly twice those of the off-resonance data (right-hand plots) due to the contribution of detector thermal noise. The means of the distributions in Fig. 4 are shown in Fig. 5, in which the data from the separate lock-in amplifier channels are plotted against each other as in Fig. 3. The on- and off-resonance means agree within the 1σ standard deviations shown, indicating the absence of any resonant force signal. The offset from the origin of the mean of the off-resonance distribution is due to leakage of the reference signal internal to the lock-in.

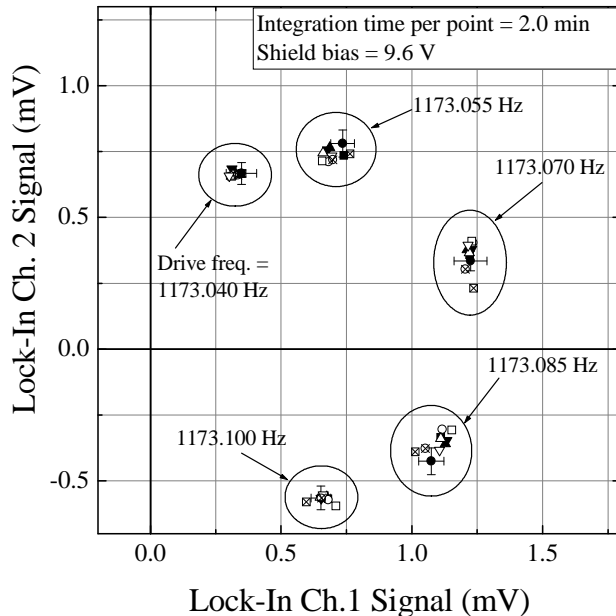


FIG. 3: Data from the biased runs of 10 consecutive cycles of the data sample. Points from separate cycles are labeled with unique symbols. 1σ error bars are shown for one cycle. Groups of points corresponding to a particular drive frequency are circled.

B. Consistency Checks

After the acquisition of the session data, several checks are made to verify the stability of the results and their consistency with known backgrounds. First, several additional cycles are acquired with variations in the test mass geometry, including larger vertical gaps and different overlap configurations. No resonant signal is observed in any of these sessions. This strongly disfavors the possibility that the observed null result is due to a fortuitous cancellation of surface potential, magnetic, and/or acoustic effects, all of which are expected to have different dependencies on the geometry.

Next, several on-resonance runs are acquired with different transducer probe bias voltage settings and with the source mass drive turned off. The observed linear dependence of the rms fluctuation in these data on the probe bias voltage is consistent with detector motion due only to thermal noise and rules out additional motion from transducer back-action noise. This check is important because the magnitude of the detector thermal motion is used for

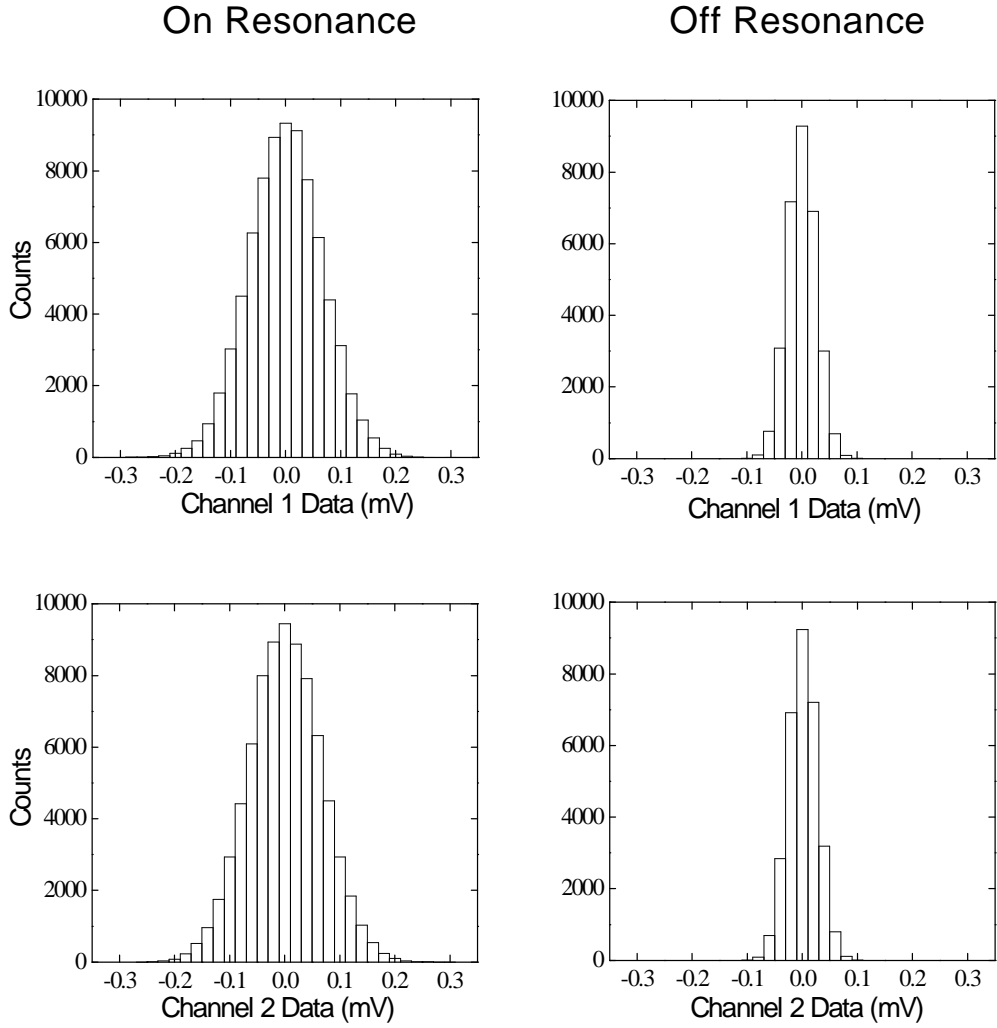


FIG. 4: Distributions of data samples without shield bias. Left-hand plots: Drive (and lock-in reference) tuned to detector resonance. Right-hand plots: Drive tuned 2 Hz below detector resonance.

calibration.

The data from the diagnostic runs with shield bias voltage applied can be used to estimate the minimum size of the residual potential difference between the shield and the (grounded)

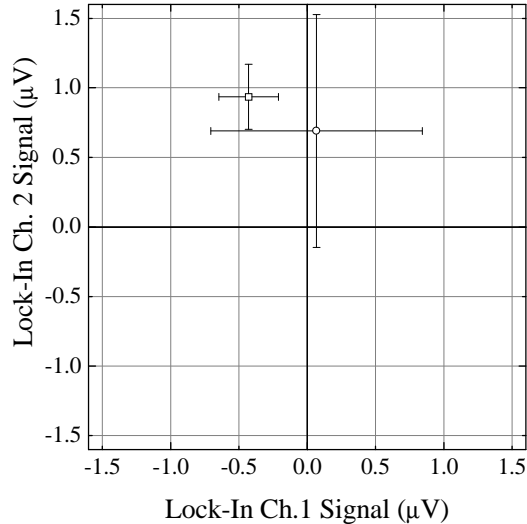


FIG. 5: Means of the distributions in Fig. 4. with channels plotted against each other to show phase. Error bars are 1σ standard deviations of the means. The point with the larger error bars is the on-resonance mean.

test masses needed to produce a resonant signal. From Fig. 3, the maximum signal with 9.6 V shield bias is about 1.3 mV. Further measurements show that this signal scales as the fourth power of the shield bias voltage, as expected for an electrostatic force between source and detector mediated by a deflected shield. Scaling the ratio of the on-resonance error bar in Fig. 5 to the 1.3 mV diagnostic implies that a residual shield bias of at least 1.5 V would be needed to generate a systematic effect above detector thermal noise. This is about an order of magnitude larger than the measured residual potential difference between the shield and test masses.

Magnetic effects can generate background signals through several mechanisms. The most important effect involves generation of eddy currents when the source mass moves in an external magnetic field. Fields produced by the source eddy currents create eddy currents in the detector, which then interact with the applied field. Studies of this effect with large applied fields show that the induced force varies as the square of the applied field (as expected), and extrapolation to the ambient field actually present indicates that this effect should be about 5 times smaller than the thermal noise limited sensitivity.

C. Auxiliary Measurements

Before acquiring the session data samples, several measurements are made to support the analysis of the data for evidence of a net force. These include the relative phases of the motion of the test masses, the detector mechanical quality factor, and a precise survey of the test mass geometry.

The Yukawa interaction for the test mass geometry of the experiment is used to model any potential signal. Such an interaction can result in either a purely attractive or repulsive force between the source and detector masses. In order to ascertain the phase of the signal for such a force, the source and detector are placed in their fiducial positions with an additional vertical offset so that both are situated above the electrostatic shield. An electrostatic bias of 1.5 V is applied to the detector mass with a dry cell in order to induce a large, stable, purely attractive electrostatic coupling between the test masses. A set of runs is taken with small increments of the PZT drive frequency between successive runs. The position of the data point in the complex plane corresponding to the maximum signal as a function of drive frequency is recorded. The phase of this signal corresponds to that of a purely attractive force. The phase of a purely attractive signal is 189° , just below the negative horizontal axis in the plots in Figs. 3 and 5.

The detector mechanical quality factor Q is measured by applying a 100 mV resonant ac signal directly to the detector, switching the detector to ground, and observing the ring-down signal on the lock-in amplifier with the reference frequency tuned 1 Hz off the detector resonance. A value for Q is obtained from a least-squares fit to the ring-down waveform. Several such measurements are made before and after the data cycles reported here, yielding a Q of 25522 ± 29 .

In the initial step of the test mass geometry survey, the source and detector masses are positioned over the electrostatic shield. The source is tilted on its horizontal axes to ensure that the front left corner is the lowest point on the bottom surface. This corner is then used as a probe to make a map of the top surface of the detector mass, using a square grid of points with a point density of 1.0 mm^{-2} . The tilt stage of the detector mass is then adjusted to optimize the level of the detector, and the surface is mapped again. A similar procedure is then carried out for the electrostatic shield. Finally, a map of the bottom surface of the source mass is obtained by touching this surface off against the sapphire hemisphere probe

fixed to the end of the shield mount. The level is optimized with the source mass tilt stage, and the map is repeated.

In order to obtain the modeshape and amplitude of the driven source mass, the PZT is driven at the resonance of the detector and another grid of points is obtained by touching the bottom surface of the source mass against the sapphire probe. These measurements are done at atmospheric pressure and the touch-offs are determined acoustically.

The system is then closed and brought down to diffusion pump pressure. The relative horizontal positions of the source and detector masses are determined by touching an edge of the source against an edge of the detector, and then the horizontal positions are set to the fiducial locations. Next, the source is lowered to bring the test masses into momentary contact, and their vertical and horizontal positions are recorded. The detector mass is then positioned under the electrostatic shield. First it is brought as far forward under the shield as possible (without the detector and shield stacks making physical contact), then centered between the sides of the shield mount as determined by touch-off signals. The same net horizontal translations required to position the detector are applied to the source, bringing the test masses into their fiducial positions.

Finally, the minimum vertical gap is established. The top surface of the detector is brought into momentary contact with the bottom surface of the shield, then backed off by 20 μm . The bottom surface of the source is brought into momentary contact with the top surface of the shield, and the source is backed off by 20 μm (the amplitude at the end of the source mass) plus an additional 10 μm for safety.

D. Calibration

Conversion of the voltage data to observed force is achieved by direct comparison of the mean signal to thermal noise. Comparison of the root mean square thermal oscillations of the detector mass to the mean displacement of the detector when driven by the source mass leads to the expression

$$\overline{V^D} = \sqrt{\overline{|V^T|^2}} \frac{Q}{\omega_0 \sqrt{k_B T} \rho_d} \frac{\int d^3 \vec{r}^{\#} \vec{z}^F(\vec{r}^{\#}) \cdot \vec{f}(\vec{r}^{\#})}{\sqrt{\int d^3 \vec{r}^{\#} |\vec{z}^F(\vec{r}^{\#})|^2}}, \quad (2)$$

where $\overline{V^D}$ is the mean of the distribution of voltages in the data sample, $\sqrt{\overline{|V^T|^2}}$ is the component of the standard deviation of the same data sample due to detector thermal

noise, k_B is Boltzmann's constant, and Q, ω_0, T , and ρ_d are the detector mechanical quality factor, resonant frequency, temperature, and density. Both $\overline{V^D}$ and $\sqrt{|\overline{V^T}|^2}$ are evaluated at a phase of 189° , corresponding to a purely attractive force. The expression $\vec{z}^F(\vec{r}') \cdot \vec{f}(\vec{r}')$ is the projection of the driving force density $\vec{f}(\vec{r}')$ times the free modal displacement $\vec{z}^F(\vec{r}')$ of the detector at arbitrary point \vec{r}' on the detector, and $|\vec{z}^F(\vec{r}')|^2$ the mean square free modal displacement; both are integrated over the detector volume. A derivation of Eq. 2 is given in Appendix A. This expression can be used to convert $\overline{V^D}$ directly to observed force. Alternately, the instrument may be calibrated using a calculable electrostatic force or by using the reciprocity of the transducer. Both methods agree with calibration based on the thermal motion, but the uncertainties involved are substantially larger.

IV. ANALYSIS

Generally, the constraints on the Yukawa parameter α for a given range λ are obtained by ascertaining how large of a Yukawa interaction between the test masses could be present and still be consistent with the data in Fig. 5. We present first a simplified analysis based on an idealized geometry and neglecting all systematic effects. As the data are consistent with a null result limited by detector thermal noise, this preliminary estimate can be made by comparing the hypothetical Yukawa force between the source and detector with the detector thermal noise.

Following the previous analysis of this experiment in Ref. [6], the detector modeshape is taken to be a pure rotation and the source mass motion a pure translation normal to its surface. The source mass is driven at the detector resonant frequency, and only the Fourier amplitude of the Yukawa torque at this frequency is effective in driving the detector. From Ref. [6], the torque amplitude is

$$|N_Y(\omega_0)| = 2\pi\alpha G\rho_d\rho_s A_d R\lambda^2 I_1(dz_s/\lambda) \exp(-g_{sd}/\lambda)[1 - \exp(-t_d/\lambda)][1 - \exp(-t_s/\lambda)]. \quad (3)$$

Here, ρ_s is the source mass density, A_d is the area of the detector under the source mass (half the area of the small rectangle), R is the distance from the edge of the detector to the torsion axis (equal to $w_d/2$; see Table II below), dz_s is the source mass amplitude, g_{sd} is the average source–detector gap, $I_1(dz_s/\lambda)$ is the modified Bessel function, and t_d and t_s are the detector and source thicknesses. This expression neglects edge effects and does not include

the true cantilever modeshape of the source mass.

The thermal noise torque in the experimental bandwidth on the small detector rectangle is found from the mechanical Nyquist expression:

$$N_T = \sqrt{\frac{4k_B T}{\tau} \left(\frac{mR^2\omega_0}{3Q} \right)}. \quad (4)$$

Here, m is the mass of the small rectangle, τ is the inverse of the bandwidth, and Q is the detector quality factor.

The signal-to-noise ratio is the ratio of Eq. 3 to Eq. 4. Setting this equal to unity and solving for α yields an approximation to the experimental limit curve shown in Fig. 7. Evaluating this expression using the mean values of the parameters listed in Tables I and II below, assuming an integration time of 77760 s and an average source amplitude equal to 1/2 the measured tip amplitude, yields a limit in the (α, λ) space stronger than the result in Fig. 7 by a small numerical factor for ranges $\lambda > 50 \mu\text{m}$. The discrepancy increases to about two orders of magnitude at $\lambda = 5 \mu\text{m}$ due to the high sensitivity of the Yukawa exponential to systematic errors in the source amplitude and the average gap.

To take the precise geometry and the systematic error into account, the Yukawa force between the test masses is computed numerically and constraints on the Yukawa strength α in Fig. 7 are calculated using a maximum likelihood technique [22]. In this approach, the interval $[\alpha_{\text{lo}}, \alpha_{\text{up}}]$ which contains the true value of α with probability CL is given by

$$CL = \int_{\alpha_{\text{lo}}}^{\alpha_{\text{up}}} p(\alpha|\mathbf{x})d\alpha, \quad (5)$$

where $p(\alpha|\mathbf{x})$ is the posterior probability density function (p.d.f.) for α given the experimental data \mathbf{x} . The posterior p.d.f. is in turn calculated from Bayes' theorem,

$$p(\alpha|\mathbf{x}) = \frac{L(\mathbf{x}|\alpha)\pi(\alpha)}{\int_{-\infty}^{\infty} L(\mathbf{x}|\alpha')\pi(\alpha')d\alpha'}, \quad (6)$$

where $L(\mathbf{x}|\alpha)$ is the likelihood function and $\pi(\alpha)$ is the prior p.d.f. for α .

In order to account for the effects of various systematics such as test mass geometry, density, and other mechanical properties, the likelihood function in Eq. 6 is replaced by the expression

$$L'(\mathbf{x}|\alpha) = \int L(\mathbf{x}|\alpha, \boldsymbol{\nu})\pi(\boldsymbol{\nu})d\boldsymbol{\nu}, \quad (7)$$

where $\boldsymbol{\nu}$ represents the set of systematic variables and $\pi(\boldsymbol{\nu})$ is their prior p.d.f.. In Eq. 7, $L(\boldsymbol{x}|\alpha, \boldsymbol{\nu})$ is given by

$$L(\boldsymbol{x}|\alpha, \boldsymbol{\nu}) = \left(\frac{1}{\sigma\sqrt{2\pi e}} \right)^N \exp \left[-\frac{(\bar{x} - \mu(\alpha, \boldsymbol{\nu}))^2}{2(\sigma/\sqrt{N})^2} \right], \quad (8)$$

where \bar{x} is the average of the voltages \boldsymbol{x} in the data session, σ is their standard deviation, and N is the effective number of uncorrelated samples. The term $\mu(\alpha, \boldsymbol{\nu})$ is the *predicted* mean voltage for a given α and set of systematics $\boldsymbol{\nu}$. It is equivalent to $\overline{V^D}$ in Eq. 2, where $\vec{f}(\vec{r}')$ in that equation is understood to be the *theoretical* value of the Yukawa force density for the experimental test mass geometry. A more detailed expression for the likelihood function is derived in Appendix B.

A. Evaluation of the Likelihood Function

Eq. 7 is evaluated by Monte Carlo integration over the systematics $\boldsymbol{\nu}$. For a fixed value of the Yukawa range λ , 400 points are thrown in the sample space defined by the volume $d\boldsymbol{\nu}$; the integrand is calculated for each point and added to a running total.

The parameter \bar{x} in Eq. 8 represents the mean of the on-resonance data with respect to the mean of the off-resonance data (which measures the effective zero), at the phase corresponding to the predicted signal. To find \bar{x} , all data are first projected onto the phase of the purely attractive signal. The mean of the off-resonance data is then subtracted from that of the on-resonance data. The value of \bar{x} obtained is $-0.44 \mu\text{V}$.

The quantity σ/\sqrt{N} , equal to the standard deviation of the mean of the data, is calculated in the following way: First, the projected data sets are partitioned into N_{part} sets of equal samples, with N_{part} large enough so that there is very little correlation between partitions. The data in each of the partitions are averaged separately and the standard deviation of the resulting averages σ_{av} is computed. The standard deviation of the mean is then calculated from $\sigma_{\text{av}}/\sqrt{N_{\text{part}}}$. The effective number of uncorrelated samples is the value of N required to make $\sigma/\sqrt{N} = \sigma_{\text{av}}/\sqrt{N_{\text{part}}}$. Finally, values of σ/\sqrt{N} obtained separately for the on- and off-resonance data sets are added in quadrature. The resulting value of σ/\sqrt{N} is $0.82 \mu\text{V}$.

A list the parameters $\boldsymbol{\nu}$ needed to evaluate Eq. 2 is given in Table I. Table II lists additional systematics which specify the test mass geometry used in the computation of the integral $\int d^3\vec{r}' \vec{z}^F(\vec{r}') \cdot \vec{f}(\vec{r}')$ in Eq. 2.

All parameters in Tables I and II are listed with their mean value and error. As the information about most of the ν is limited, a uniform p.d.f. centered about the mean with a width equal to twice the error is assumed for each of the priors $\pi(\nu)$.

The quantities G , k_B , ρ_d , and ρ_s are taken from tabulated values [23]. To obtain the thermal noise $\sqrt{|V^T|^2}$, the standard deviation of the off-resonance data (that is, the noise due to the JFET amplifier) is subtracted in quadrature from the standard deviation of the on-resonance data. The error on $\sqrt{|V^T|^2}$ is estimated in the same way as the standard deviation of the mean σ/\sqrt{N} of the projected data sets.

Several measurements of the detector mechanical quality factor Q were made immediately before and after the data sessions, with the test masses in their fiducial positions. The values in Table I represent the resulting average and standard deviation of these measurements.

The quantity $\sqrt{\int d^3\vec{r}^{\prime} |z^F(\vec{r}^{\prime})|^2}$ in Eq. 2, the root mean square free modeshape of the detector integrated over its volume, is computed numerically from a complete finite element model of the detector mass and is treated as a single systematic with a uniform error of 10%. The free modeshape is normalized to a maximum amplitude of $1 \mu m$.

For a particular set of the ν in Table II, a value of the expression $\int d^3\vec{r}^{\prime} z^F(\vec{r}^{\prime}) \cdot \vec{f}'(\vec{r}^{\prime})$ in Eq. 2 is obtained in a separate Monte Carlo integration. In this calculation, the detector curvature, source mass curvature and source mass modeshape are described by second order polynomials obtained from fits to the survey data. The detector modeshape is described by

TABLE I: Systematics in Eq. 2 for evaluation of likelihood function

Parameter	Mean	Error	Units
Gravitational constant, G	6.673×10^{-11}	1.0×10^{-13}	$m^3 kg^{-1} s^{-2}$
Boltzmann constant, k_B	$1.3806503 \times 10^{-23}$	2.4×10^{-29}	J K ⁻¹
Detector density (tungsten), ρ_d	1.93×10^4	1.9×10^3	kg m ⁻³
Source density (tungsten), ρ_s	1.93×10^4	1.9×10^3	kg m ⁻³
Thermal noise voltage, $\sqrt{ V^T ^2}$	6.09×10^{-5}	2.3×10^{-6}	V
Mechanical quality factor, Q	2.5522×10^4	29	(NA)
Resonant frequency, $\omega_0/2\pi$	1173.085	0.015	Hz
Temperature, T	305.0	0.1	K
Integrated rms free modeshape, $\sqrt{\int d^3\vec{r}^{\prime} z^F(\vec{r}^{\prime}) ^2}$	5.87×10^{-11}	5.9×10^{-12}	m ^{5/2}

TABLE II: Systematics for evaluation of $\int d^3\vec{r}' \vec{z}^F(\vec{r}') \cdot \vec{f}(\vec{r}')$. All units are meters. See text for definition of parameters.

Parameter	Mean	Error
Detector length, l_d	5.0800×10^{-3}	6.4×10^{-6}
Detector width, w_d	1.14550×10^{-2}	6.4×10^{-6}
Detector thickness, t_d	1.950×10^{-4}	6.4×10^{-6}
Source width, w_s	7.0000×10^{-3}	6.4×10^{-6}
Source thickness, t_s	3.048×10^{-4}	6.4×10^{-6}
Touch gap, g_{sd}	1.080×10^{-4}	6.4×10^{-6}
Source amplitude, dz_s	1.87×10^{-5}	3.2×10^{-6}

a similar function obtained from the finite element model. The curvature and modeshape functions and the ν are used to calculate bounding boxes for the source mass and the small rectangle of the detector mass. For a particular position of the source mass, 1×10^5 point pairs are thrown. For those pairs landing within the bounding boxes a force density $\vec{f}(\vec{r}')$ is calculated and added to a running total. A total of 30 different phase positions of the source mass between 0 and 2π radians are sampled, with the range defined by the amplitude dz_s .

The vertical separation of the test masses is computed from the touch gap, the test mass thicknesses (t_d, t_s), and a correction calculated from the functions describing the test mass surface curvature. The touch gap (g_{sd}) is the vertical difference in test mass positions between where the opposing test mass surfaces touch and where they are in their fiducial positions. The error on these quantities is taken to be twice the resolution of the translation stages, or $6.4 \mu\text{m}$, as two measurements are needed to determine each. This is also the case for the errors in the test mass widths (w_d, w_s) and detector length (l_d). An exception is the source mass tip amplitude (dz_s), which is the average of five measurements. Also, the accuracy with which the tip of the source mass is aligned with the back edge of the small detector rectangle is 320 microns, as it is aligned by eye and taken to have an error corresponding to a complete turn of the translation stage screw. The accuracy with which the long edge of the source mass is aligned to the torsion axis is the usual 6.4 microns, as this position is determined from touch-offs. All geometry measurements are repeatable over several weeks to within the resolution of the translation stages.

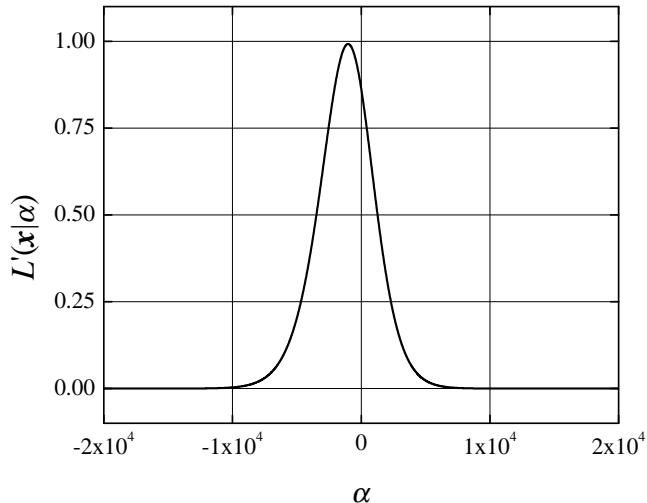


FIG. 6: Likelihood function (Eq. 7) dependence on α for the case $\lambda = 20 \mu\text{m}$.

Fig. 6 shows the likelihood function (Eq. 7) as a function of α for the case $\lambda = 20 \mu\text{m}$, a range at which the experiment has good sensitivity relative to previous experiments. The factor $(\sigma\sqrt{2\pi e})^{-N}$ has been suppressed as it has no bearing on the posterior p.d.f. for α (Eq. 6). The maximum is shifted slightly toward negative (repulsive) values of α , in accordance with the offset of the mean of the on-resonance data with respect to the off-resonance data (Fig. 5).

B. Limits on Yukawa Parameters

The function in Fig. 6 is substituted into Eq. 6 and integrated numerically (Eq. 5) over an interval $[\alpha_{\text{lo}}, \alpha_{\text{up}}]$ to obtain the limit on α . The interval is centered around the maximum of the likelihood function and the length adjusted by trial and error to obtain a confidence level of 95%. In Eq. 6, a uniform prior distribution for α is used. For the case $\lambda = 20 \mu\text{m}$, the resulting 95% confidence interval is $[-5.60 \times 10^3 < \alpha < 3.56 \times 10^3]$.

The likelihood function is recomputed and the integration repeated for several values of λ between $5 \mu\text{m}$ and $500 \mu\text{m}$. The resulting 95% confidence level limit curve in the (α, λ) parameter space is shown in Fig. 7. For each value of λ , the slightly weaker limit corresponding to a repulsive interaction is shown. The new limit is close to three orders of magnitude more sensitive than the previous experimental limits in the range between 10

and $100 \mu\text{m}$.

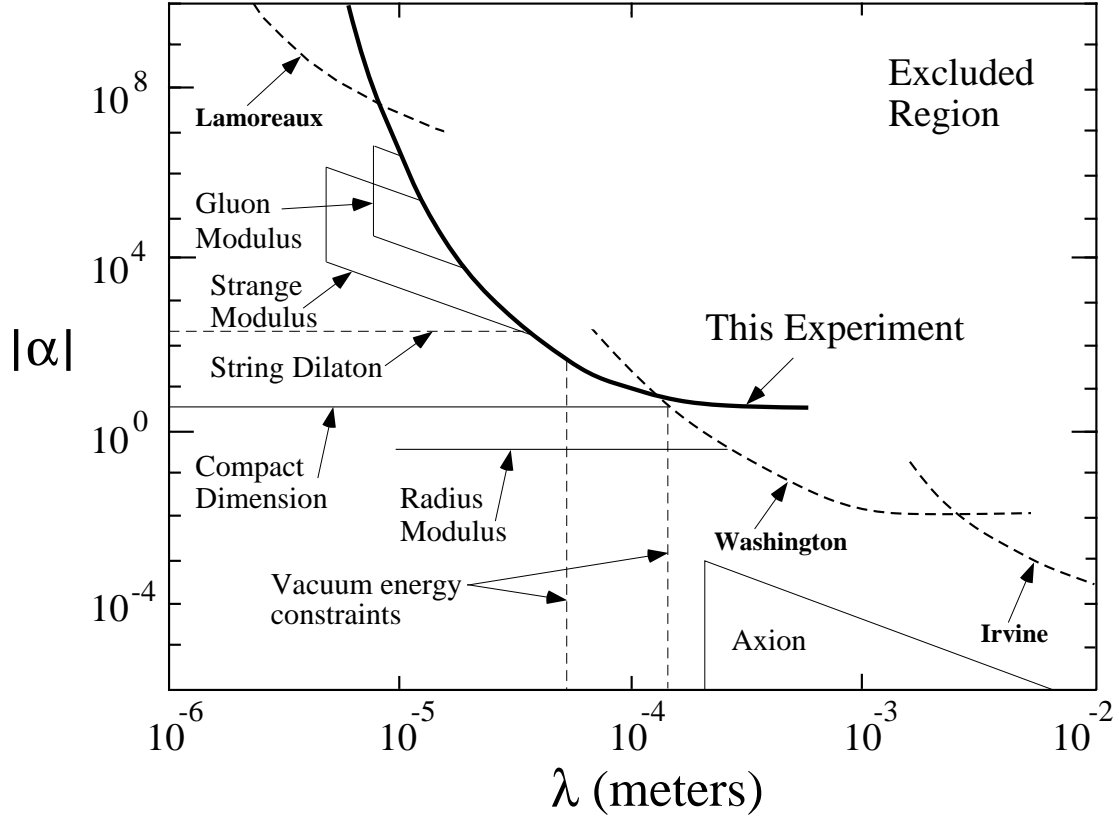


FIG. 7: 95% confidence level limit on the Yukawa strength α as a function of the range λ for this experiment (bold solid curve), together with limits from previous experiments (bold dashed curves) and theoretical predictions (fine lines).

V. CONCLUSION

An experimental search for new macroscopic forces at short distances has been conducted using 1 kHz mechanical oscillators as test masses with a stiff conducting shield between them. No evidence for a resonant signal above detector thermal noise has been observed. Based on these measurements, roughly three new square decades in the (α, λ) parameter space are ruled out in the range $10 \mu\text{m} < \lambda < 100 \mu\text{m}$. About half of the remaining parameter space for the gluon and strange modulus forces is now excluded. Our limit crosses the predicted line for the dilaton at 36 microns, corresponding to a lower limit on the dilaton mass of $1.7 \times 10^{-2} \text{ eV}$.

From Fig. 7, the sensitivity of the experiment maximizes at about 4 times gravitational strength above $\lambda = 200 \mu\text{m}$. For the planar test mass geometry of the current experiment, the Newtonian signal is roughly an order of magnitude below the thermal noise at this range. Detection of this signal should be possible with more statistics and an optimized geometry. The small test masses in this experiment allow for relatively easy control of the minimum separation, currently limited to $100 \mu\text{m}$ by the thickness of the electrostatic shield. Preliminary tests with stretched metal membranes suggest that shields of sufficiently low compliance can be made with thicknesses as small as $10 \mu\text{m}$. Work is underway toward an experiment with a stretched membrane shield in place of the sapphire plate. If the backgrounds can be controlled, this experiment could improve limits between 10 and $50 \mu\text{m}$ by at least another order of magnitude.

Acknowledgments

The authors would like to thank Elizabeth Lagae for her continuing work in the laboratory, and Cole Briggs, Tracy Buxkemper, Leslie Czaia, Hans Green, Sid Gustafson, and Hans Rohner of the University of Colorado and JILA instrument shops for technical assistance. This work is supported by NSF grant PHY00-71029.

APPENDIX A: CALIBRATION

The mean signal from the lock-in amplifier data can be converted to observed force by direct comparison to the detector thermal noise. The mean square thermal displacement of the detector mass $\overline{|\bar{z}^T(\vec{r})|^2}$ at the position \vec{r} of the capacitive transducer probe is related to the temperature T via the equipartition theorem:

$$\frac{1}{2}m(\vec{r})\overline{|\bar{z}^T(\vec{r})|^2}\omega_0^2 = \frac{1}{2}k_B T. \quad (\text{A1})$$

Here, ω_0 is the resonant frequency of the 5th detector mode and $m(\vec{r})$ is the modal mass of the detector oscillator at the position of the probe.

For a distributed mass with free modal displacement $\bar{z}^F(\vec{r}')$ at an arbitrary point \vec{r}' driven on resonance, the driven displacement amplitude $d\bar{z}^D(\vec{r}')$ due to a differential force amplitude

$d\vec{F}(\vec{r}') is given by$

$$d\vec{z}^D(\vec{r}') = -j \frac{Q}{\omega_0^2 m(\vec{r}')} \vec{z}^F(\vec{r}') \frac{\vec{z}^F(\vec{r}') \cdot d\vec{F}(\vec{r}')}{|\vec{z}^F(\vec{r}')|^2}, \quad (\text{A2})$$

where Q is the detector mechanical quality factor and the dot product picks out the component of the force parallel to the modal displacement. (Note the use of $e^{+j\omega t}$ time dependence.)

The differential amplitude at the probe is

$$d\vec{z}^D(\vec{r}') = |d\vec{z}^D(\vec{r}')| \frac{\vec{z}^F(\vec{r}')}{|\vec{z}^F(\vec{r}')|}. \quad (\text{A3})$$

Substituting Eq. A3 into Eq. A2 and integrating over \vec{r}' yields the amplitude of the detector at the position of the transducer due the total force on the detector:

$$\vec{z}^D(\vec{r}) = -j \frac{Q}{\omega_0^2 \rho_d} \vec{z}^F(\vec{r}) \frac{\int d^3\vec{r}' \vec{z}^F(\vec{r}') \cdot \vec{f}(\vec{r}')}{\int d^3\vec{r}' |\vec{z}^F(\vec{r}')|^2}. \quad (\text{A4})$$

Here the force amplitude density $\vec{f}(\vec{r}')$ is defined by $\vec{f}(\vec{r}') \equiv d\vec{F}(\vec{r}')/d^3\vec{r}'$, ρ_d is the detector mass density, and the definition of the modal mass

$$m(\vec{r}) = \frac{\rho_d \int |\vec{z}^F(\vec{r}')|^2 d^3\vec{r}'}{|\vec{z}^F(\vec{r}')|^2} \quad (\text{A5})$$

has been used.

Combining Eqs. A1, A4, and A5 yields

$$\frac{\vec{z}^D(\vec{r})}{\sqrt{|\vec{z}^T(\vec{r})|^2}} = \frac{Q}{j\omega_0 \sqrt{k_B T} \rho_d} \frac{\vec{z}^F(\vec{r})}{|\vec{z}^F(\vec{r})|} \frac{\int d^3\vec{r}' \vec{z}^F(\vec{r}') \cdot \vec{f}(\vec{r}')}{\sqrt{\int d^3\vec{r}' |\vec{z}^F(\vec{r}')|^2}}. \quad (\text{A6})$$

The linear response of the capacitive transducer insures that the ratio $\vec{z}^D(\vec{r})/\sqrt{|\vec{z}^T(\vec{r})|^2}$ is related to the measured voltages on the lock-in amplifier by

$$\frac{|\vec{z}^D(\vec{r})|}{\sqrt{|\vec{z}^T(\vec{r})|^2}} = \frac{\overline{V^D}}{\sqrt{|V^T|^2}}, \quad (\text{A7})$$

where $\overline{V^D}$ is the mean of the distribution of voltages in the data sample and $\sqrt{|V^T|^2}$ is the component of the standard deviation of the same data sample due to detector thermal noise. Both quantities are evaluated at the phase of interest. Substitution of Eq. A7 into Eq. A6 yields Eq. 2.

APPENDIX B: LIKELIHOOD FUNCTION

In addition to the unknown parameter α corresponding to the Yukawa strength, the signal depends on a set of systematics $\boldsymbol{\nu}$ which includes test mass geometry, density, detector temperature and mechanical properties. The effects of uncertainties in these quantities can be accounted for in the posterior p.d.f. (Eq. 6) by integrating over the systematics:

$$p(\alpha|\mathbf{x}) = \int p(\alpha, \boldsymbol{\nu}|\mathbf{x})d\boldsymbol{\nu}. \quad (\text{B1})$$

Assuming the prior joint p.d.f. for α and $\boldsymbol{\nu}$ factorizes, this is equivalent to replacing the likelihood function $L(\mathbf{x}|\alpha)$ with

$$L'(\mathbf{x}|\alpha) = \int L(\mathbf{x}|\alpha, \boldsymbol{\nu})\pi(\boldsymbol{\nu})d\boldsymbol{\nu}. \quad (\text{B2})$$

Here, $\pi(\boldsymbol{\nu})$ is the prior p.d.f. of the $\boldsymbol{\nu}$. The function $L(\mathbf{x}|\alpha, \boldsymbol{\nu})$ is the joint p.d.f. for the data, regarded as a function of both the unknown Yukawa strength α and the systematics $\boldsymbol{\nu}$:

$$L(\mathbf{x}|\alpha, \boldsymbol{\nu}) = \prod_i F(x_i|\alpha, \boldsymbol{\nu}). \quad (\text{B3})$$

For the present experiment, the data x_i are the sampled voltages from the lock-in amplifier, which are Gaussian distributed (Fig. 4). Therefore the function F is taken to be the Gaussian distribution $G(x_i|\mu(\alpha, \boldsymbol{\nu}), \sigma)$, where $\mu(\alpha, \boldsymbol{\nu})$ is the *predicted* mean voltage for a given α and set of systematics $\boldsymbol{\nu}$, and σ is the observed standard deviation:

$$F(x_i|\alpha, \boldsymbol{\nu}) = \left(\frac{1}{\sigma\sqrt{2\pi}} \right) \exp \left[-(x_i - \mu(\alpha, \boldsymbol{\nu}))^2/2\sigma^2 \right]. \quad (\text{B4})$$

The product is

$$\begin{aligned} \prod_i F(x_i|\alpha, \boldsymbol{\nu}) &= \left(\frac{1}{\sigma\sqrt{2\pi}} \right)^N \exp \left[-\frac{1}{2\sigma^2} \sum_{i=1}^N (x_i - \mu(\alpha, \boldsymbol{\nu}))^2 \right] \\ &= \left(\frac{1}{\sigma\sqrt{2\pi e}} \right)^N \exp \left[-\frac{(\bar{x} - \mu(\alpha, \boldsymbol{\nu}))^2}{2(\sigma/\sqrt{N})^2} \right], \end{aligned} \quad (\text{B5})$$

where \bar{x} is the average of the voltages x_i and N is the effective number of uncorrelated samples (the value of N such that σ/\sqrt{N} is the standard deviation of the mean of the actual data).

The predicted mean $\mu(\alpha, \boldsymbol{\nu})$ can be replaced by Eq. 2 for $\overline{V^D}$ if $\vec{f}(\vec{r}^*)$ is identified with the *theoretical* value of the Yukawa force density for a test mass geometry corresponding to

a particular set of parameters $\boldsymbol{\nu}$. As a Yukawa force density, $\vec{f}(\vec{r}')$ is linear in the parameter α , the gravitational constant G , and the source mass and detector mass densities ρ_s and ρ_d : $\vec{f}(\vec{r}') = \alpha G \rho_s \rho_d \vec{f}(\vec{r}')$. Substituting into Eq. 2 and factoring these terms out of the integral yields

$$\mu(\alpha, \boldsymbol{\nu}) = (\alpha G \rho_s \sqrt{\rho_d}) \sqrt{|V^T|^2} \left(\frac{Q}{\omega_0 \sqrt{k_B T}} \right) \frac{\int d^3 \vec{r}' \vec{z}^F(\vec{r}') \cdot \vec{f}(\vec{r}')}{\sqrt{\int d^3 \vec{r}' |\vec{z}^F(\vec{r}')|^2}}. \quad (\text{B6})$$

Substituting Eq. B6 into Eq. B5 and the result into Eq. B2 yields the likelihood function $L'(\boldsymbol{x}|\alpha)$.

-
- [1] E. G. Adelberger, et al., hep-ex/0202008; C. D. Hoyle, et al., Phys Rev. Lett. 86 (2002) 1418.
 - [2] E. Fischbach and C. Talmadge, The Search for Non-Newtonian Gravity (New York, Springer-Verlag, 1999) 62.
 - [3] M. Bordag, U. Mohideen, and V. M. Mostepanenko, Phys. Rep. 353 (2001) 1; E. Fischbach, D. E. Krause, V. M. Mostepanenko, and M. Novello, Phys. Rev. D 64 (2001) 075010.
 - [4] J. K. Hoskins, R. D. Newman, R. Spero, and J. Schultz, Phys. Rev. D 32 (1985) 3084.
 - [5] S. K. Lamoreaux, Phys. Rev. Lett. 78 (1997) 5.
 - [6] J. C. Long, H. W. Chan, and J. C. Price, Nucl. Phys. B 539 (1999) 23.
 - [7] Another estimate (Ref. [3] above) which considers corrections to the Casimir force not considered by the authors, such as those for surface roughness and finite temperature, suggests this limit to be about an order of magnitude more sensitive.
 - [8] The summary given here is by no means exhaustive. The electronic references to N. Arkani-Hamed, et al., hep-ph/9803315 provide a more current and comprehensive resource.
 - [9] J. Hewett and M. Spiropulu, hep-ph/0205106, submitted Annu. Rev. Nucl. Part. Sci. (2002).
 - [10] N. Arkani-Hamed, S. Dimopoulos, and G. Dvali, Phys. Lett. B 429 (1998) 263.
 - [11] E. G. Floratos and G. K. Leontaris, Phys. Lett. B 465 (1999) 95; A. Kehagias and K. Sfetsos, Phys. Lett. B 472 (2000) 39.
 - [12] S. Dimopoulos and G. Giudice, Phys. Lett. B 379 (1996) 105.
 - [13] I. Antoniadis, S. Dimopoulos, and G. Dvali, Nucl. Phys. B 516 (1998) 70.
 - [14] J. Ellis, et al., Phys. Lett. B 228 (1989) 264.
 - [15] D. B. Kaplan and M. B. Wise, J. High Energy Phys. 8 (2000) 37.

- [16] L. J. Rosenberg and K. A. van Bibber, *Phys. Rep.* 325 (2000) 1.
- [17] E. Fischbach and D. E. Krause, *Phys. Rev. Lett.* 82 (1999) 4753.
- [18] R. Sundrum, *J. High Energy Phys.* 7 (1999) 1.
- [19] S. R. Beane, *Gen. Rel. Grav.* 29 (1997) 945.
- [20] R. N. Kleiman, et al., *Rev. Sci. Instrum.* 56 (1985) 2088.
- [21] H. W. Chan, J. C. Long, and J. C. Price, *Rev. Sci. Instrum.* 70 (1999) 2742-50.
- [22] K. Hagiwara et al., *Phys. Rev. D* 66 (2002) 010001 sec. 31.4.
- [23] K. Hagiwara et al., *Phys. Rev. D* 66 (2002) 010001 secs. 1, 6.